Search for time-independent neutrino emission from astrophysical sources with 3 years of IceCube data.

M. G. Aartsen[b], R. Abbasi[aa], Y. Abdou[v], M. Ackermann[ap], J. Adams[o],
J. A. Aguilar[u], M. Ahlers[aa], D. Altmann[i], J. Auffenberg[aa], X. Bai[ae,1],
M. Baker[aa], S. W. Barwick[w], V. Baum[ab], R. Bay[g], J. J. Beatty[q,r],
S. Bechet[l], J. Becker Tjus[j], K.-H. Becker[ao], M. L. Benabderrahmane[ap],
S. BenZvi[aa], P. Berghaus[ap], D. Berley[p], E. Bernardini[ap], A. Bernhard[ad],
D. Z. Besson[y], G. Binder[h,g], D. Bindig[ao], M. Bissok[a], E. Blaufuss[p],
J. Blumenthal[a], D. J. Boersma[an], S. Bohaichuk[t], C. Bohm[ah], D. Bose[m],
S. Böser[k], O. Botner[an], L. Brayeur[m], H.-P. Bretz[ap], A. M. Brown[o],
R. Bruijn[x], J. Brunner[ap], M. Carson[v], J. Casey[e], M. Casier[m], D. Chirkin[aa],
A. Christov[u], B. Christy[p], K. Clark[am], F. Clevermann[s], S. Coenders[a],
S. Cohen[x], D. F. Cowen[am,al], A. H. Cruz Silva[ap], M. Danninger[ah],
J. Daughhetee[e], J. C. Davis[q], M. Day[aa], C. De Clercq[m], S. De Ridder[v],
P. Desiati[aa], K. D. de Vries[m], M. de With[i], T. DeYoung[am],
J. C. Díaz-Vélez[aa], M. Dunkman[am], R. Eagan[am], B. Eberhardt[ab],
J. Eisch[aa], S. Euler[a], P. A. Evenson[ae], O. Fadiran[aa], A. R. Fazely[f],
A. Fedynitch[j], J. Feintzeig[aa], T. Feusels[v], K. Filimonov[g], C. Finley[ah],
T. Fischer-Wasels[ao], S. Flis[ah], A. Franckowiak[k], K. Frantzen[s], T. Fuchs[s],
T. K. Gaisser[ae], J. Gallagher[z], L. Gerhardt[h,g], L. Gladstone[aa],
T. Glüsenkamp[ap], A. Goldschmidt[h], G. Golup[m], J. G. Gonzalez[ae],
J. A. Goodman[p], D. Góra[ap], D. T. Grandmont[t], D. Grant[t], A. Groß[ad],
C. Ha[h,g], A. Haj Ismail[v], P. Hallen[a], A. Hallgren[an], F. Halzen[aa],
K. Hanson[l], D. Heereman[l], D. Heinen[a], K. Helbing[ao], R. Hellauer[p],
S. Hickford[o], G. C. Hill[b], K. D. Hoffman[p], R. Hoffmann[ao], A. Homeier[k],
K. Hoshina[aa], W. Huelsnitz[p,2], P. O. Hulth[ah], K. Hultqvist[ah], S. Hussain[ae],
A. Ishihara[n], E. Jacobi[ap], J. Jacobsen[aa], K. Jagielski[a], G. S. Japaridze[d],
K. Jero[aa], O. Jlelati[v], B. Kaminsky[ap], A. Kappes[i], T. Karg[ap], A. Karle[aa],
J. L. Kelley[aa], J. Kiryluk[ai], J. Kläs[ao], S. R. Klein[h,g], J.-H. Köhne[s],
G. Kohnen[ac], H. Kolanoski[i], L. Köpke[ab], C. Kopper[aa], S. Kopper[ao],

[1]Physics Department, South Dakota School of Mines and Technology, Rapid City, SD 57701, USA

[2]Los Alamos National Laboratory, Los Alamos, NM 87545, USA

[3]also Sezione INFN, Dipartimento di Fisica, I-70126, Bari, Italy

[4]NASA Goddard Space Flight Center, Greenbelt, MD 20771, USA

D. J. Koskinen[am], M. Kowalski[k], M. Krasberg[aa], K. Krings[a], G. Kroll[ab],
J. Kunnen[m], N. Kurahashi[aa], T. Kuwabara[ae], M. Labare[v], H. Landsman[aa],
M. J. Larson[ak], M. Lesiak-Bzdak[ai], M. Leuermann[a], J. Leute[ad],
J. Lünemann[ab], O. Macías[o], J. Madsen[ag], G. Maggi[m], R. Maruyama[aa],
K. Mase[n], H. S. Matis[h], F. McNally[aa], K. Meagher[p], M. Merck[aa],
T. Meures[l], S. Miarecki[h,g], E. Middell[ap], N. Milke[s], J. Miller[m],
L. Mohrmann[ap], T. Montaruli[u,3], R. Morse[aa], R. Nahnhauer[ap],
U. Naumann[ao], H. Niederhausen[ai], S. C. Nowicki[t], D. R. Nygren[h],
A. Obertacke[ao], S. Odrowski[ad], A. Olivas[p], A. Omairat[ao], A. O'Murchadha[l],
L. Paul[a], J. A. Pepper[ak], C. Pérez de los Heros[an], C. Pfendner[q], D. Pieloth[s],
E. Pinat[l], J. Posselt[ao], P. B. Price[g], G. T. Przybylski[h], L. Rädel[a],
M. Rameez[u], K. Rawlins[c], P. Redl[p], R. Reimann[a], E. Resconi[ad], W. Rhode[s],
M. Ribordy[x], M. Richman[p], B. Riedel[aa], J. P. Rodrigues[aa], C. Rott[aj],
T. Ruhe[s], B. Ruzybayev[ae], D. Ryckbosch[v], S. M. Saba[j], T. Salameh[am],
H.-G. Sander[ab], M. Santander[aa], S. Sarkar[af], K. Schatto[ab], F. Scheriau[s],
T. Schmidt[p], M. Schmitz[s], S. Schoenen[a], S. Schöneberg[j], A. Schönwald[ap],
A. Schukraft[a], L. Schulte[k], O. Schulz[ad], D. Seckel[ae], Y. Sestayo[ad],
S. Seunarine[ag], R. Shanidze[ap], C. Sheremata[t], M. W. E. Smith[am],
D. Soldin[ao], G. M. Spiczak[ag], C. Spiering[ap], M. Stamatikos[q,4], T. Stanev[ae],
A. Stasik[k], T. Stezelberger[h], R. G. Stokstad[h], A. Stößl[ap], E. A. Strahler[m],
R. Ström[an], G. W. Sullivan[p], H. Taavola[an], I. Taboada[e], A. Tamburro[ae],
A. Tepe[ao], S. Ter-Antonyan[f], G. Tešić[am], S. Tilav[ae], P. A. Toale[ak],
S. Toscano[aa], E. Unger[j], M. Usner[k], S. Vallecorsa[u], N. van Eijndhoven[m],
A. Van Overloop[v], J. van Santen[aa], M. Vehring[a], M. Voge[k], M. Vraeghe[v],
C. Walck[ah], T. Waldenmaier[i], M. Wallraff[a], Ch. Weaver[aa], M. Wellons[aa],
C. Wendt[aa], S. Westerhoff[aa], N. Whitehorn[aa], K. Wiebe[ab],
C. H. Wiebusch[a], D. R. Williams[ak], H. Wissing[p], M. Wolf[ah], T. R. Wood[t],
K. Woschnagg[g], D. L. Xu[ak], X. W. Xu[f], J. P. Yanez[ap], G. Yodh[w],
S. Yoshida[n], P. Zarzhitsky[ak], J. Ziemann[s], S. Zierke[a], M. Zoll[ah]

[a]*III. Physikalisches Institut, RWTH Aachen University, D-52056 Aachen, Germany*
[b]*School of Chemistry & Physics, University of Adelaide, Adelaide SA, 5005 Australia*
[c]*Dept. of Physics and Astronomy, University of Alaska Anchorage, 3211 Providence Dr.,*
Anchorage, AK 99508, USA
[d]*CTSPS, Clark-Atlanta University, Atlanta, GA 30314, USA*
[e]*School of Physics and Center for Relativistic Astrophysics, Georgia Institute of*
Technology, Atlanta, GA 30332, USA
[f]*Dept. of Physics, Southern University, Baton Rouge, LA 70813, USA*
[g]*Dept. of Physics, University of California, Berkeley, CA 94720, USA*
[h]*Lawrence Berkeley National Laboratory, Berkeley, CA 94720, USA*

[i]Institut für Physik, Humboldt-Universität zu Berlin, D-12489 Berlin, Germany

[j]Fakultät für Physik & Astronomie, Ruhr-Universität Bochum, D-44780 Bochum, Germany

[k]Physikalisches Institut, Universität Bonn, Nussallee 12, D-53115 Bonn, Germany

[l]Université Libre de Bruxelles, Science Faculty CP230, B-1050 Brussels, Belgium

[m]Vrije Universiteit Brussel, Dienst ELEM, B-1050 Brussels, Belgium

[n]Dept. of Physics, Chiba University, Chiba 263-8522, Japan

[o]Dept. of Physics and Astronomy, University of Canterbury, Private Bag 4800, Christchurch, New Zealand

[p]Dept. of Physics, University of Maryland, College Park, MD 20742, USA

[q]Dept. of Physics and Center for Cosmology and Astro-Particle Physics, Ohio State University, Columbus, OH 43210, USA

[r]Dept. of Astronomy, Ohio State University, Columbus, OH 43210, USA

[s]Dept. of Physics, TU Dortmund University, D-44221 Dortmund, Germany

[t]Dept. of Physics, University of Alberta, Edmonton, Alberta, Canada T6G 2E1

[u]Département de physique nucléaire et corpusculaire, Université de Genève, CH-1211 Genève, Switzerland

[v]Dept. of Physics and Astronomy, University of Gent, B-9000 Gent, Belgium

[w]Dept. of Physics and Astronomy, University of California, Irvine, CA 92697, USA

[x]Laboratory for High Energy Physics, École Polytechnique Fédérale, CH-1015 Lausanne, Switzerland

[y]Dept. of Physics and Astronomy, University of Kansas, Lawrence, KS 66045, USA

[z]Dept. of Astronomy, University of Wisconsin, Madison, WI 53706, USA

[aa]Dept. of Physics and Wisconsin IceCube Particle Astrophysics Center, University of Wisconsin, Madison, WI 53706, USA

[ab]Institute of Physics, University of Mainz, Staudinger Weg 7, D-55099 Mainz, Germany

[ac]Université de Mons, 7000 Mons, Belgium

[ad]T.U. Munich, D-85748 Garching, Germany

[ae]Bartol Research Institute and Department of Physics and Astronomy, University of Delaware, Newark, DE 19716, USA

[af]Dept. of Physics, University of Oxford, 1 Keble Road, Oxford OX1 3NP, UK

[ag]Dept. of Physics, University of Wisconsin, River Falls, WI 54022, USA

[ah]Oskar Klein Centre and Dept. of Physics, Stockholm University, SE-10691 Stockholm, Sweden

[ai]Department of Physics and Astronomy, Stony Brook University, Stony Brook, NY 11794-3800, USA

[aj]Department of Physics, Sungkyunkwan University, Suwon 440-746, Korea

[ak]Dept. of Physics and Astronomy, University of Alabama, Tuscaloosa, AL 35487, USA

[al]Dept. of Astronomy and Astrophysics, Pennsylvania State University, University Park, PA 16802, USA

[am]Dept. of Physics, Pennsylvania State University, University Park, PA 16802, USA

[an]Dept. of Physics and Astronomy, Uppsala University, Box 516, S-75120 Uppsala, Sweden

[ao]Dept. of Physics, University of Wuppertal, D-42119 Wuppertal, Germany

[ap]DESY, D-15735 Zeuthen, Germany

Abstract

We present the results of a search for neutrino point sources using the Ice-Cube data collected between April 2008 and May 2011 with three partially completed configurations of the detector: the 40-, 59- and 79-string configurations. The live-time of this data set are 1,040 days. An unbinned maximum likelihood ratio test was used to search for an excess of neutrinos above the atmospheric background at any given direction in the sky. By adding two more years of data with improved event selection and reconstruction techniques, the sensitivity was improved by a factor 3.5 or more with respect to the previously published results [11] obtained with the 40-string configuration of IceCube. We performed an all-sky survey and a dedicated search using a catalog of *a priori* selected objects observed by other telescopes. In both searches, the data are compatible with the background-only hypothesis. In the absence of evidence for a signal, we set upper limits on the flux of muon neutrinos. For an E^{-2} neutrino spectrum, the observed limits are between 0.9 and 23.2×10^{-12} TeV^{-1} cm^{-2}s^{-1}. We also report upper limits for neutrino emission from groups of sources which were selected according to theoretical models or observational parameters and analyzed with a stacking approach.

Keywords: astroparticle physics − cosmic rays − neutrinos − telescopes

1. Introduction

The origin and the acceleration mechanisms of Cosmic Rays (CRs) are a yet unresolved puzzle. The random-walk of CR particles through the intergalactic magnetic fields makes it difficult to identify the cosmological sources of CRs except at the highest energies. On the other hand, neutrinos are likely produced in the same environments as CRs and gamma-rays and, being electrically neutral, they propagate directly from the source to the Earth. Since these astrophysical neutrinos also have directional information, their detection will make it possible to unequivocally identify the sources of CRs. Possible sources may be Supernova Remnant (SNR) shocks, Active Galactic Nuclei (AGN) jets or Gamma-Ray Bursts (GRBs) [1, 2]. The detection of high-energy cosmic neutrinos will provide a direct proof of hadronic particle acceleration in the Universe since they can only be produced by the

4

interactions of protons or nuclei with ambient radiation or matter.

In this paper we present the latest results of the search for neutrino point sources with the IceCube neutrino observatory. The analysis was done on the data collected from 2008 to 2011. This paper concerns the searches for steady neutrino sources while optimized searches for time-dependent neutrino emission are reported elsewhere [3].

Section 2 describes the IceCube detector and the detection principle. The three data samples and the corresponding event selections are discussed in Sec. 3. The methodology used to combine data from different years and detector configurations in a point source search is given in Sec. 4 while Sec. 5 presents the results of the analysis, including a discussion of their impact on some recent astrophysical models of neutrino emission. The systematic uncertainties are described in Sec. 6 and conclusions are drawn in Sec. 7.

2. Detector

The IceCube detector at the South Pole is designed to observe neutrinos of astrophysical origin and atmospheric muons and neutrinos induced by Cosmic Rays at the energies around and above the *knee* ($\sim 3 \times 10^{15}$ eV).

IceCube detects the Cherenkov light emitted by secondary leptons which are produced in charged current neutrino interactions with the matter surrounding the detector and is hence sensitive to all neutrino flavors. For neutrino point source searches we select events from charged current interactions of muon neutrinos since they result in secondary muons with long tracks and a good directional reconstruction. Above TeV energies, the scattering angle between the muon and the incoming neutrino is smaller than the angular resolution of the detector. In order to detect the Cherenkov light, IceCube uses an array of 5,160 Digital Optical Modules (DOMs) [4] deployed on 86 strings at a depth of 1.5-2.5 km below the surface just above the bedrock in the clear, deep ice. The DOMs are spherical, pressure resistant glass housings containing each a 25 cm diameter Hamamatsu photomultiplier tube (PMTs) and electronics for waveform digitization [5]. High quantum efficiency PMTs are used in a denser sub-array located in the center of the detector. This sub-array, called DeepCore, enhances the sensitivity to low energy neutrinos [6]. A surface cosmic-ray detector, called IceTop, completes the IceCube Observatory [9]. It uses 324 PMTs to detect the electromagnetic component of air-showers produced by cosmic-ray interactions in the atmosphere.

The construction of the IceCube Observatory started in the Austral summer of 2004 and ended in December 2010. Data acquisition with the complete configuration started in May 2011. However, IceCube has been providing physics results since the completion of the 9-string array in 2006. From April 2008 to May 2011 three different configurations of the IceCube detector were in operation. Fig. 1 shows the positions of the strings in the 40-string configuration (IC-40) which took data from 2008 April 5 to 2009 May 20, the 59-string configuration (IC-59) active from 2009 May 20 to 2010 May 31, and the 79-string configuration (IC-79) active from 2010 May 31 to 2011 May 13. Also shown is the final 86-string IceCube configuration. The total live-time over the entire period used in this work corresponds to 1,040 days collected with the IC-40, IC-59 and IC-79 configurations and the average up-time is of 92% at final analysis level.

In this analysis we used a simple multiplicity trigger where 8 or more DOMs recorded a light deposition within a 5 μs time window (SMT8). Most of the events which are selected by this trigger are composed of muons produced by Cosmic Rays in the atmosphere above the detector (about 2.2 kHz at trigger level in the 79-string configuration). These events enter the detector only from above since muons produced in the opposite hemisphere of the atmosphere are absorbed by the Earth. Only about one in 10^6 recorded events is induced by an atmospheric neutrino which can reach IceCube from any direction. The goal of all further event selections is to increase the ratio of the neutrino signal from astrophysical sources with respect to the muon background. Key elements of the selection of the neutrino candidates are the reconstructions of the event direction and of the deposited energy. Only high quality reconstructed events are selected in order to strongly reduce the background of downward going muons that are mis-reconstructed as upward going. Moreover, since in many signal scenarios the signal is expected to have higher energy than the atmospheric background, the estimated energy can be used to suppress the low energy muon background. For instance, the first order Fermi acceleration mechanisms in SNR shocks predicts a neutrino power law spectrum of E^{-2} while the atmospheric neutrinos have a differential spectrum in energy above 100 GeV that goes as $E^{-3.7}$ [10].

A significant part of the background reduction is performed on-line at the South Pole (L1 filter) where first cuts on the quality of the reconstruction of up-going events are applied and high-energy down-going muons from the northern hemisphere are selected. This filtering of events is designed to serve a large variety of different muon neutrino searches by maintaining a high
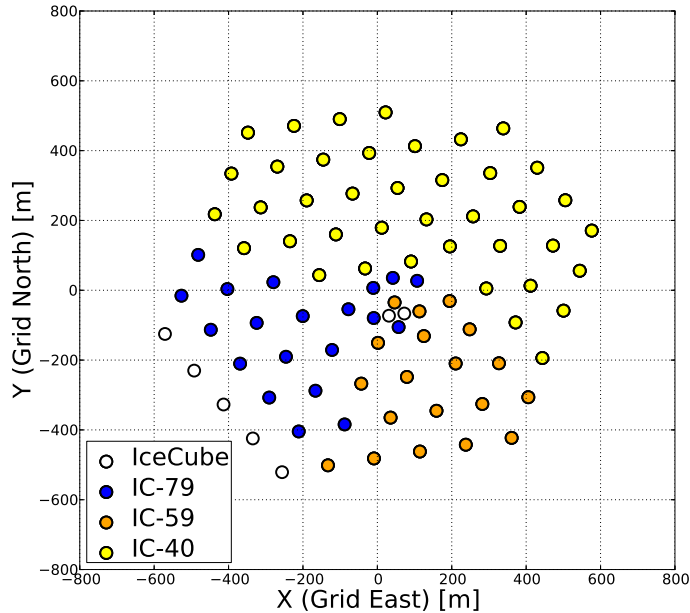
Figure 1: Detector layout in the IceCube coordinate system: The Grid North axis is aligned with the Prime Meridian, pointing towards Greenwich, UK. The Grid East axis points 90 degrees clock-wise from Grid North. The circles represent the surface string positions corresponding to the final geometry of the whole IceCube detector. The IC-40 configuration is represented by yellow dots. The green circles represent the additional strings that form the IC-59 configuration. The IC-59 configuration together with the strings indicated by blue circles represent the IC-79 configuration. The empty circles are the strings added for the complete detector.

signal efficiency. This reduction of atmospheric muon background is sufficient to send the remaining data off-site by satellite where they undergo further processing (L2 filter). Fig. 2 shows the data rate of each run as function of the modified Julian date for one of the data streams of the L2 filter, the muon filter. Also shown is the South Pole atmospheric temperature. As can be seen, the atmospheric muon rate is strongly correlated with the atmospheric density which depends on the temperature.

Most track reconstructions performed at the South Pole are likelihood based with the exception of $linefit$, which is an algorithm used as a seed for more precise and CPU intense reconstructions to follow. These likelihood-
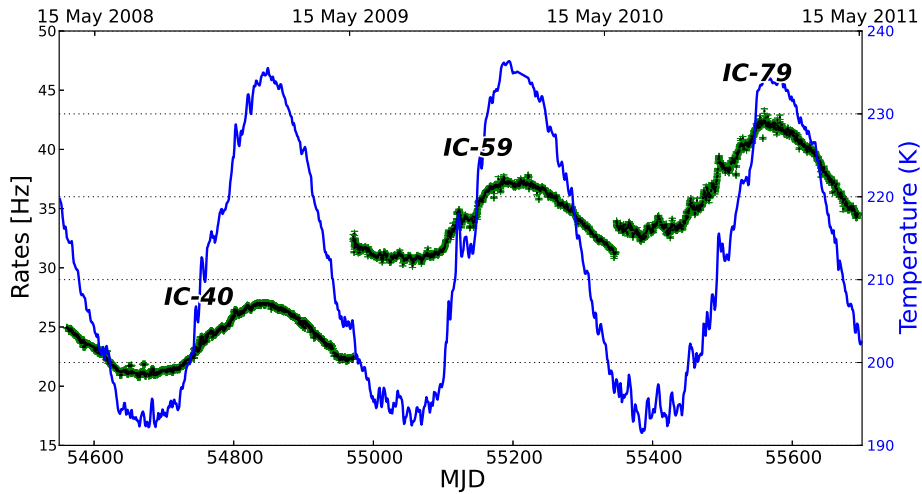
Figure 2: IceCube event rates for the three periods at the muon filter level as a function of the modified Julian date. The correlation with the effective temperature of the South Pole atmosphere is also shown. The effective temperature is a weighted average which takes into account the temperature and pressure at different levels of the atmosphere as well as the attenuation length of the pion as defined in [15].

based fits use the photon arrival time distribution for track reconstruction [12]. The multi photoelectron (MPE) likelihood function, which uses time and amplitude information of the PMT pulses, is applied after several iterations of the single photoelectron (SPE) likelihood fit that uses only the pulse leading edge time. The energy estimation is performed after the track reconstruction since the muon direction information is used by the energy reconstruction algorithm. The muon energy proxy described in [11] was used in all three years of data of this analysis together with a more recently developed algorithm described in [13] as alternative energy estimator for the data collected with the 79-string configuration.

3. Event selection

The first order background rejection of the on-line filter is not sufficient for high-level data analyses. Up-going, high-energy neutrino candidates can be selected from the data by rejecting events with a poor reconstruction since they are more likely to be down-going muons, by removing mis-reconstructed

8

events with multiple muon tracks and by suppressing events with low energies. In the southern sky, it is not possible to reject the muon background based on the reconstruction quality of the events, and the most energetic events are selected instead to improve the ratio of signal to background events [21, 11]. Reflecting the different detector geometries and the general improvement in the muon track reconstruction and identification of muon background events, we used a different event selection for each of the three periods of data used in this work.

The ability to observe a neutrino point source depends on the expected number of background events, the observable number of neutrinos for a given source strength, the energies of these events and the angular resolution. The discovery potential, defined as the flux needed to make a 5σ discovery in 50% of an ensemble of pseudo-experiments with a simulated signal of this strength, captures all these aspects and was used as the main figure of merit to optimize the event selections. Diffuse shock acceleration leads to power-law spectra with a spectral index around 2 [7, 8], and neutrinos originating in CR interactions near the source are expected to follow a similar spectrum. We thus used an E^{-2} spectrum as our main benchmark model. Several galactic γ-ray sources have energy spectra with energy cut-offs at a few TeV [14], supporting the idea that galactic neutrino spectra may present cut-off spectra as well. We therefore also took softer neutrino spectra into account. These softer spectra were modeled by larger spectral indexes (e.g. 2.7 or 3) and/or by exponential energy cut-offs.

3.1. IceCube 40-strings data sample

During the IC-40 period, IceCube was active and taking data more than 99% of the time, and 92% of the data were used after selecting periods of stable detector operation. The data used after this selection correspond to a live-time of 375.5 days. The event selection for the point source analysis of the IC-40 data was obtained by cuts on a number of well-understood and powerful variables and is described in detail in Ref. [11]. In the southern sky, events were selected with a cut on the reconstructed energy of the event which was parameterized as a function of the reconstructed declination. The final sample of events obtained from the IC-40 configuration contained a total of 36,900 events: 14,121 from the northern sky and 22,779 from the southern sky.
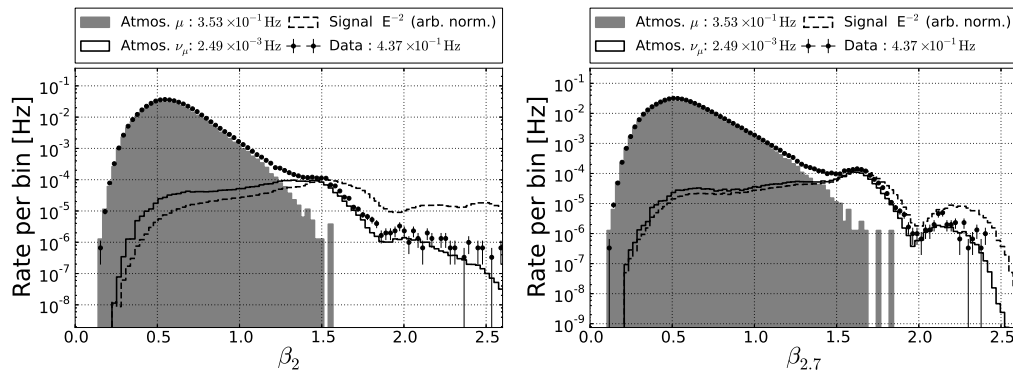
Figure 3: Distribution of the BDT score for the ensemble of trees trained with an E^{-2} spectrum (left) and an $E^{-2.7}$ spectrum (right) as signal. The data shown here are from the IC-59 configuration and examples for a signal distribution are shown with an arbitrary normalization.

3.2. IceCube 59-strings data sample

The data from the IC-59 configuration correspond to a live-time of 348.1 days. The rate of the SMT8 trigger was of the order of 1.5 kHz, and the on-line muon filter rate was a factor two higher than in the previous configuration as can be seen in Fig. 2.

It was shown in Refs. [16] and [17] that a higher efficiency for up-going neutrino events with energies below 10 TeV can be achieved with multi-variate approaches without compromising the discovery potential for neutrino sources with hard energy spectra. In the IC-59 data sample, we used Boosted Decision Trees (BDTs) [19] to this end. BDTs are widely used in two-class classification problems where a larger set of weakly discriminating variables is available [20] and are thus well-suited for the selection of neutrino events from the IceCube data.

The multivariate cuts were based on twelve observables with a high discriminating power between signal and background. We used 10% of the atmospheric muon dominated data as a background model for the BDT training. Any possible astrophysical signal contributes only a very small fraction to the data at this level. The observables were selected such that their correlation in the background-dominated data sample were below 50%. The signal was modeled with Monte Carlo simulation. Two different signal energy spectra were considered: an E^{-2} spectrum, and one with a neutrino spectrum of $E^{-2.7}$ to account for softer neutrino spectra. Additionally, the reconstructed

track was required to be within $0.5°$ of the simulated direction in order to train the BDT with only well-reconstructed events.

For computational reasons, the observables were split in two sets of eight and four variables, and a BDT was defined for each set separately. The final selection was based on a combination of the two BDT scores. Fig. 3 shows the distribution of the combined BDT scores obtained by the training with the two different signal spectra for data and a simulated neutrino signal as well as for the simulated atmospheric muon and neutrino backgrounds.

Events in the southern Hemisphere were selected with a cut on the reconstructed energy. The strength of the cut was varied as a function of the declination. In addition, we used the veto capability of the surface array IceTop [22] to reduce the muon background. Atmospheric muons are accompanied by extended air showers which can produce early hits in the IceTop surface array. The veto is defined by counting the number of detected photo electrons in IceTop within a time window around the expected arrival time of the shower front in the surface detector. In the IC-59 event selection, the Ice-Top veto was used for events with reconstructed declinations between $-90°$ and $-40°$. The best veto efficiency is expected for events with high energies, heavy primaries, vertical directions and a shower axis close to the IceTop detector. Fig. 6 shows the veto capability of the IceTop surface array using atmospheric muon dominated data from IC-79. The IceTop veto allows us to reject background with 99% efficiency in the vertically down-going region without losing signal neutrino efficiency ($\lesssim 1\%$).

The final data sample for the IC-59 configuration has a total number of 107,569 events, among which almost 2/3 come from the southern sky. The rest are neutrino candidates in the northern sky.

3.3. IceCube 79-strings data sample

As illustrated in Fig. 1, the IC-79 configuration had almost the final volume of the full IceCube detector. With the largest detector size among the configurations discussed here, the background from coincidences of two or more atmospheric muons within the same read-out window is more abundant than in the previous ones. At the same time, the number of neutrino events in coincidence with an atmospheric down-going muon increased as well. We applied a topological hit clustering based on the spatial and temporal separation of recorded PMT signals to separate neutrinos from coincident muons. In addition to the reconstruction of the full event, we applied the same reconstruction to up to three topologically connected subsets of hits. Among these
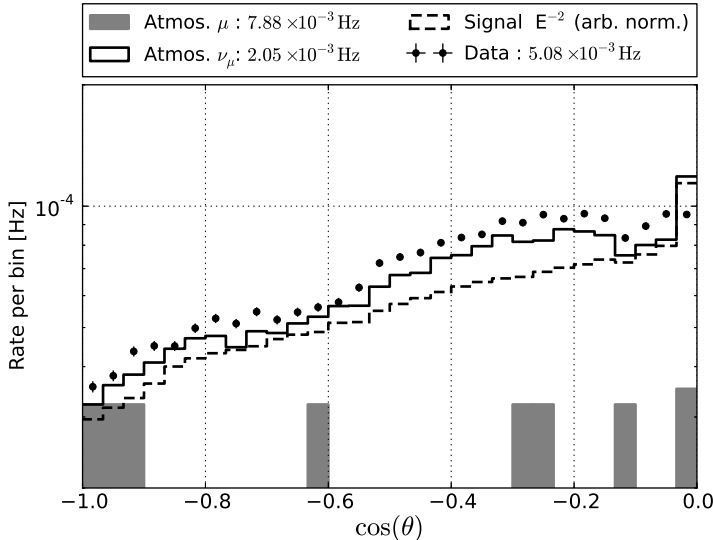
Figure 4: Zenith distribution at final cut level for the up-going neutrino selection. Points represent data. The dashed line is a benchmark E^{-2} astrophysical neutrino signal normalized to the all-sky atmospheric neutrino rate shown to illustrate how an hypothetical signal distributes in zenith. The solid line is the simulated atmospheric neutrino contribution and the filled histogram shows the simulated contribution of mis-reconstructed atmospheric muons after all cuts estimated.

and the original reconstructed track, only the most likely neutrino candidate was selected. If only the reconstruction of the full hit information passed the cuts but none of the subsets, the events were rejected to improve the background suppression. A visual inspection of more than 50 events at the final selection level showed that the topological splitting of events allowed us to select additional, high-quality neutrino events from which a coincident muon contamination was removed.

Two different high-level event selections have been developed, which we denote sample A and B in the following. While all the results presented in this article have been obtained on sample A, we used sample B for cross-checks and validation of the point source analysis.

For both event samples, we used a combination BDTs for the event selection in the northern sky and divided this area into two regions, a horizontal and a vertical one. For sample A (B), we considered events within
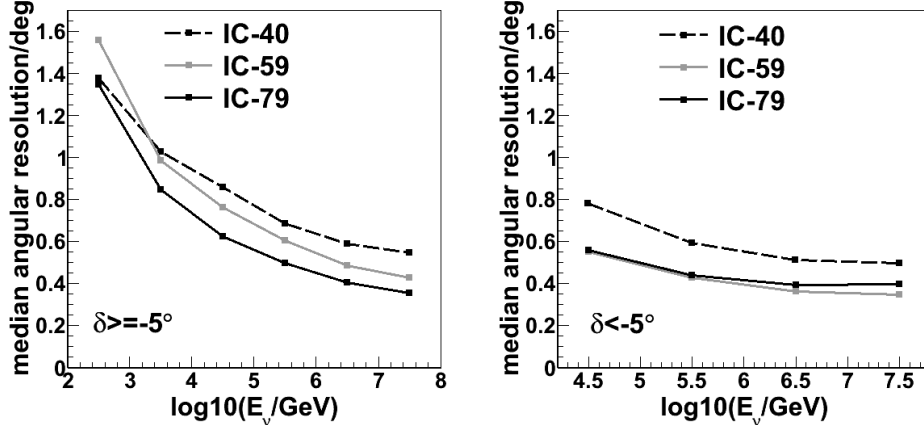
Figure 5: Neutrino angular resolution defined as the median of the point spread function of the true neutrino direction and the reconstructed muon direction for northern (right) and the southern sky (left) at analysis level.

$-5° \leq \delta \leq +40°$ ($0° \leq \delta \leq +35°$) and events within $+40° \leq \delta \leq +90°$ ($+35° \leq \delta \leq +90°$) separately. The two bands are characterized by different expected signal energy spectra due to the absorption of high-energy neutrinos in the Earth and by different distributions of the background.

For sample A, seventeen observables were selected for the BDT based on their discrimination power between a neutrino signal and the muon background. They were split into two sets of nine and eight variables each. In addition, we asked for the background and signal correlation coefficients between any two variables in the same set to be below 50%. A number of variables with less discrimination power were included since BDTs are robust against the inclusion of weak variables. The final cut parameter was defined by a combination of the two BDT scores for each zenith region.

In sample B, only highly discriminating variables were included in the BDTs and the event selection used a different number of variables in the horizontal region where the signal is dominated by higher energy events. Nine variables were selected for the vertical region and fifteen variables for the horizontal region. No requirement was applied to limit the correlations between the variables, allowing us to use all selected variables in a single BDT in each region. Eight of the observables used for the BDT sample B were also used in sample A.

As in the IC-59 selection we trained the BDTs with two different signal

spectra, using again the E^{-2} spectrum as a benchmark for hard spectra. As representative of a soft spectrum, we used an $E^{-2.4}$ spectrum with a cutoff at 7 TeV for sample A and an $E^{-2.7}$ spectrum for sample B.

The final selections were optimized to provide the best discovery potential for E^{-2} neutrino fluxes. At the same time, we aimed to achieve a near-optimal discovery potential for softer spectra by adding additional lower energy events. We also paid special care in having a smooth transition in the event rate between the two declination regions. Fig. 4 shows the zenith distribution for the up-going event selection in sample A. As can be seen, it is fully dominated by atmospheric neutrinos and only a small fraction of mis-reconstructed down-going atmospheric muons survive after the event selection.

For sample A, we extended the cuts from the up-going region to the southern hemisphere by using the same set of cuts and a retrained BDT as an intermediate event selection. In addition, an angular uncertainty estimator was required to be smaller than $2°$. We also applied a veto based rejecting events with three or more veto hits in the surface array IceTop. The probability to veto events by accidental coincidences was estimated by using experimental data from an off-time window where no correlated signal in IceTop is expected. It is below 1% at every declination and energy. The probability to veto a background event is shown in Fig. 6. The background rejection power is above 90% for high-energy, vertical down-going muons. To further decrease the rate of accidental coincidences, we applied the IceTop veto cut only in those regions of the energy-declination space where it is most efficient. In this way, the accidental veto probability is much smaller than 1% and its effect on the signal efficiency can be neglected. The effect of the Ice-Top veto in the IC-79 and IC-59 event selection is visible in Fig. 7. For very vertical down-going events ($\sin\delta < -0.85$) where the veto is most efficient there is a decrease in the discovery flux. Finally, a declination-dependent energy cut was used to select a constant number of events per solid angle and to provide a smooth transition from the northern to the southern hemisphere.

For sample B, a simple energy cut depending on the declination was applied to select a constant number of events per solid angle. The same, soft IceTop veto as above was used to reject part of the down-going atmospheric muon background at the very vertical zenith angles. A study performed on this sample indicated that no significant gain in the discovery potential could be achieved by selecting a larger number of events in the Southern Hemisphere.
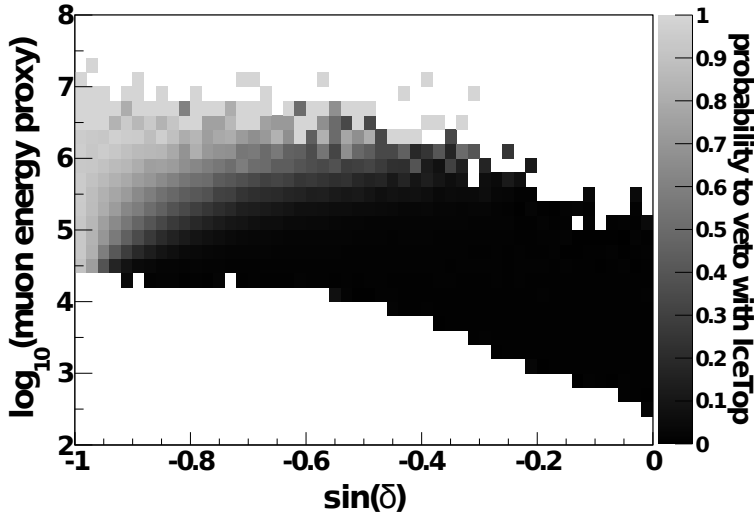
14

Figure 6: IceTop veto capability as a function of the sine of the declination, δ, of the detected muon and the estimated energy of the detected muon in the detector based on the data from IC-79. The events used for this visualization passed an intermediate set of event selection criteria but are still dominated by atmospheric muons. Events with 3 or more veto hits within a time window of ± 1000 ns around the expected shower front arrival time are rejected. 10% of the experimental data were used for this plot and the white areas correspond to regions where no event was observed.

Sample A contains 109,866 events of which 50,857 are coming from the northern sky and 59,009 are located in the southern sky.

The two samples yield the same discovery potential for steady, point-like neutrino sources both for hard (represented by an E^{-2} neutrino signal spectrum) and soft (represented by an E^{-3} neutrino signal spectrum) neutrino spectra at every declination (see Fig. 7). The differences are smaller than the statistical uncertainty of the estimation. This is a confirmation of the validity of the independent BDT selections.

Sample B has a slightly larger effective area for events at lower energies than sample A at the cost of a higher muon contamination in the northern hemisphere. Considering events with reconstructed declinations above 0°, we observe that the events which are contained in both samples make up 75% of the events in sample A and 67% of the events in sample B. The difference in the percentages reflects the smaller number of events in sample A.
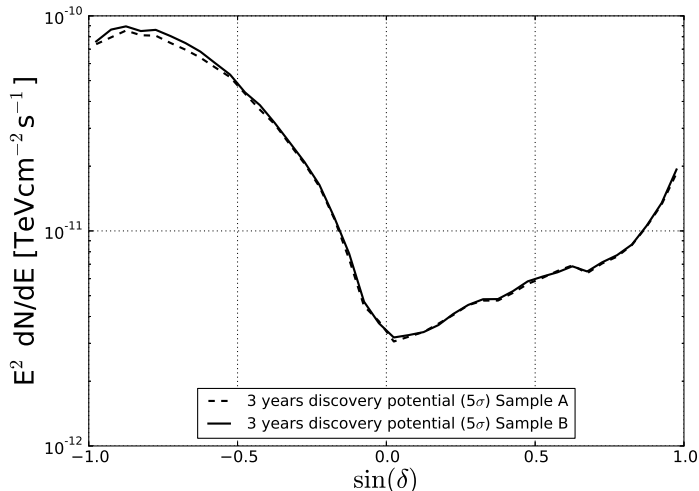
Figure 7: Discovery potential for point sources at 5σ confidence level for an E^{-2} spectrum as a function of declination for the 3 years of IceCube when sample A (dashed) or sample B (solid) is used for the IC-79 data.

The overlap between the two samples is larger for events with small angular uncertainties, rising to 81% of the events in sample A and 90% of sample B being contained in both samples if events with angular uncertainty estimates smaller than 0.5° are considered. Thus, the probability for a more signal-like, well-reconstructed event to be in both samples is higher than the corresponding probability for an event with a poor reconstruction. A visual inspection of the hit patterns of a subset of the events confirms that the contribution of background events from atmospheric muons is smaller in the group of events which are in both samples. In particular, we have visually checked the hit patterns of more than 100 up-going events which are in both samples and have an angular uncertainty estimate smaller than 0.5°; all of these were well-reconstructed up-going, i.e. neutrino-induced events.

The overlap of the two event samples in the southern sky is much smaller than in the northern sky. In the region from declination $-90°$ to $0°$, we observed that 38% of the events in sample A are also contained in sample B and that 27% of the events in sample B are also in sample A. The fraction of events common in both samples increases for smaller angular uncertainty estimates. The smaller overlap is expected. The event selection in A disfavors

16

events with very large energy losses with respect to the event selection B. Moreover, both event selections apply a filtering of different strength before the energy cut is applied on the steeply falling spectrum. Moving the strength of the energy cut at any declination by a small amount will decrease the overlap between two event selections significantly.
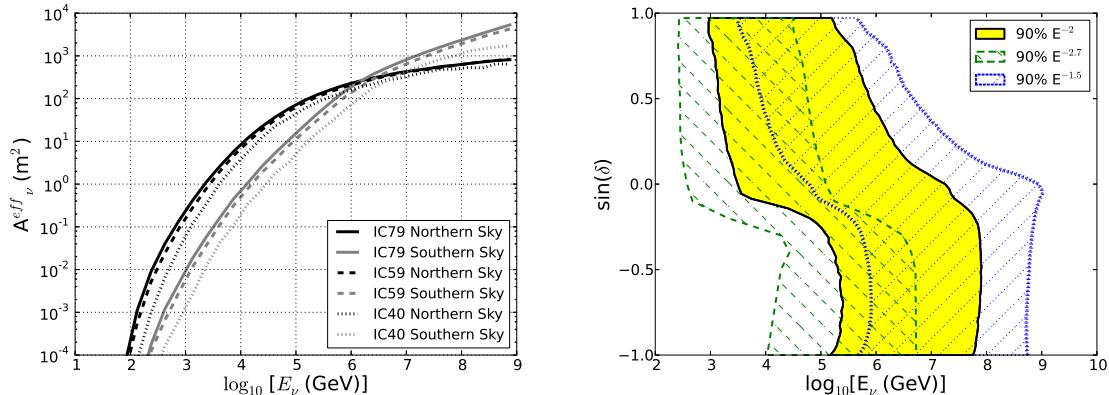

Figure 8: Left: Solid-angle-averaged muon neutrino effective area for the three event selections corresponding to three IceCube configurations for both the northern and southern skies. Right: 90% central signal containment region for three different power-law neutrino spectra as a function of declination for the three configurations combined.

Table 1 summarizes the live-time, the estimated rate of atmospheric neutrinos and the number of up-going and down-going track events in the three different configurations using sample A for the IC-79 configuration. Fig. 5 shows the neutrino angular resolution in each of the three data samples. In the northern sky, the best angular resolution is observed in IC-79. The lowest energy bin in the IC-40 sample has a better resolution than in the IC-59 sample because of the stricter event filtering applied in this energy range. The southern sky selection of the IC-59 sample applies stronger cuts than the IC-79 selection, leading to a slightly better angular resolution in this range. The effective area for muon neutrinos, A^ν_{eff}, after the final event selection for the three configurations of IceCube is shown in Fig. 8 left. For the tabulated data of this figure see the appendix Appendix A. The right panel in Fig. 8 shows the 90% central signal containment for three power-law neutrino spectrum of E^{-2}, $E^{-2.4}$ and $E^{-1.5}$ using the combination of the three different detector geometries. These regions indicate the sensitivity range of IceCube for different spectral indexes. The effect in sensitivity for point

17

sources of neutrinos can be clearly seen in Fig. 9. The dashed line represents the expected sensitivity at the 90% confidence level (C.L.) as a function of declination for an E^{-2} signal in the energy range between 10 TeV and 1 PeV where most of the signal deposition is expected for this spectrum. The dotted and solid lines show the sensitivity for an E^{-2} in a higher and lower energy range. As can be seen, IceCube's sensitivity for low energy neutrinos ($E \leq$ 10 TeV) is mostly restricted to the northern sky while at higher energies the sensitivity of the detector is more symmetric.
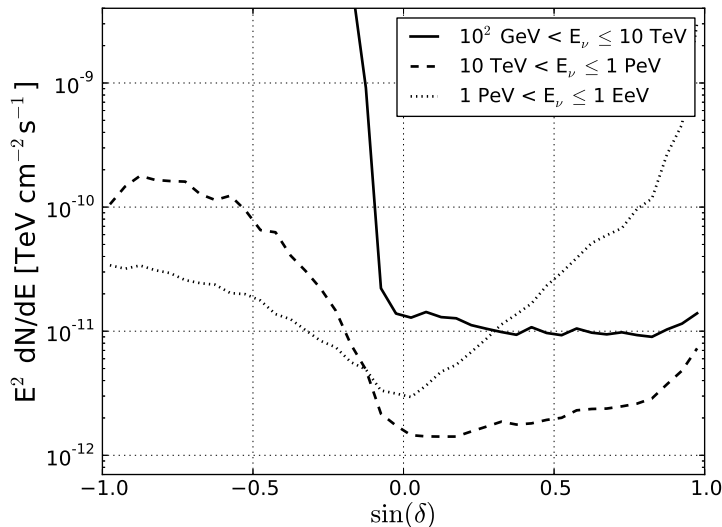

Figure 9: Sensitivity for muon neutrino flux for a E^{-2} spectrum for a 90% C.L. as a function of declination combining the three years of data averaged over right ascension. The three different lines indicate three different energy ranges.

4. The likelihood search method

To search for neutrino point sources in IceCube we use an unbinned maximum likelihood ratio test. This method follows the one described in [24] and is extended to combine different detector geometries. It calculates the significance of an excess of neutrinos over the atmospheric background by using both the directional information of the events and the energy to separate hard-spectrum signals from the softer spectra of atmospheric neutrinos and muons. The method models the expected neutrino signal from a point source

18

Table 1: Summary for three different IceCube configurations for point source analyses: The expected atmospheric neutrino rate from MC simulation weighted for the model in Ref. [23] and numbers of up- and down-going events at final selection level. The numbers for the IC-79 are from sample A.

no. of strings	live-time [days]	atm. νs	# up-going	# down-going
40	376	40/day	14,121	22,779
59	348	120/day	43,339	64,230
79	316	180/day	50,857	59,009

in the sky using simulation and since this search is background dominated its estimate is done using real data.

The signal and background probability density functions (p.d.f.) are a function of the reconstructed declination and the reconstructed muon energy.

For a data sample of N total events the p.d.f of the ith event in the jth sample (in our case the IC-40, IC-59 or IC-79 datasets) with reconstructed energy E_i and located at an angular distance to the source of $|\vec{x}_i - \vec{x}_s|$ is given by:

$$P_i^j(|\vec{x}_i - \vec{x}_s|, E_i, \gamma, n_s^j) = \frac{n_s^j}{N^j}\mathcal{S}_i^j + \left(1 - \frac{n_s^j}{N^j}\right)\mathcal{B}_i^j, \tag{1}$$

where $\mathcal{S}_i^j$ and $\mathcal{B}_i^j$ are the signal and background p.d.f. respectively and n_s^j is the fraction of total number of signal events, n_s, that is expected from the corresponding j^{th} sample.

For time integrated searches the signal p.d.f. $\mathcal{S}_i^j$ is given by:

$$\mathcal{S}_i^j = S_i^j(|\vec{x}_i - \vec{x}_s|, \sigma_i)\mathcal{E}_i^j(E_i, \delta_i, \gamma), \tag{2}$$

here S_i^j is the space contribution and depends on the angular uncertainty of the event, σ_i, and the angular difference between the reconstructed direction of the event and the source. We model this probability as a 2-dimensional Gaussian,

$$S_i^j = \frac{1}{2\pi\sigma_i^2}e^{-\frac{|\vec{x}_i - \vec{x}_s|^2}{2\sigma_i^2}}. \tag{3}$$

The energy p.d.f., $\mathcal{E}_i^j$, in the case of signal, is a function of the recon-structed energy proxy, E_i, and the spectral index, γ, of a power-law spectrum

for a given declination (see Fig. 10).

The background p.d.f., $\mathcal{B}_i^j$, is obtained from the experimental data and is given by:

$$\mathcal{B}_i^j = B_i^j(\delta_i)\mathcal{E}_i^j(E_i, \delta_i). \qquad (4)$$

The space term, $B_i^j(\delta_i)$, is the event density per unit solid angle as a function of the declination. The background density is right ascension independent due to the Earth's rotation. The energy p.d.f. for background, $\mathcal{E}_i^j$, represents the probability of obtaining an energy E_i from atmospheric backgrounds (neutrinos and muons) and therefore depends only on the declination.

The signal is considered to have the same spectrum for all data sets and therefore the spectral index meets the condition of $\gamma_j = \gamma$. The fitted numbers of signal events n_s^j in each sample are also fixed relative to each other, according to the signal hypothesis tested and the resulting fraction, $f^j(\gamma, \delta)$, of total signal events expected in each sample. Simulation is used to calculate this fraction of signal events coming from each data set for a given a spectral index, so that $n_s^j = f^j n_s$ (see Fig. 11). In this way, the likelihood, $\mathcal{L}$, remains a function of only the global parameters n_s and γ with respect to which it is maximized:

$$\mathcal{L}(\gamma, n_s) = \prod_j \mathcal{L}^j(\gamma, n_s^j) = \prod_j \prod_{i \in j} \left[\frac{n_s^j}{N^j}\mathcal{S}_i^j + \left(1 - \frac{n_s^j}{N^j}\right)\mathcal{B}_i^j\right], \qquad (5)$$

where $i \in j$ indicates that the ith-event is in sample j. The test-statistic, TS, is calculated from the likelihood ratio of the background-only (null) hypothesis over the best fitted signal-plus-background hypothesis:

$$TS = -2\log\left[\frac{\mathcal{L}(n_s = 0)}{\mathcal{L}(\hat{n}_s, \hat{\gamma})}\right]. \qquad (6)$$

Here, $\hat{n}_s$ is the best fit number of source events, and $\hat{\gamma}$ is the best fit spectral index. In principle, n_s may be positive or negative since both positive and negative fluctuations with respect to the background expectation may be observed. In the likelihood maximization however, it is constrained to non-negative values. Pseudo-experiments on randomized data are performed to determine the significance of the observation. The randomization is achieved by the assignment of a random right ascension to each event in the data
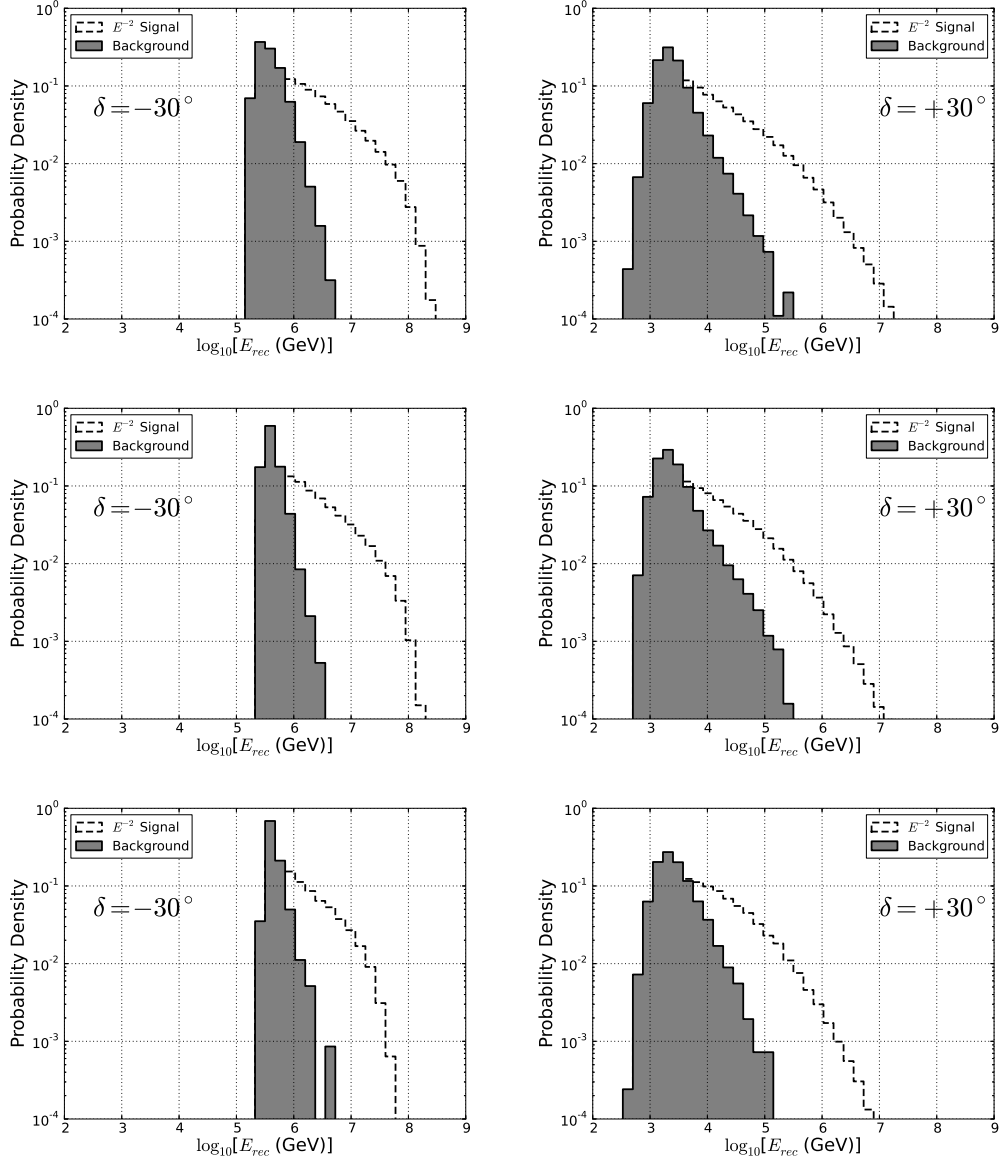
20

Figure 10: Energy p.d.f. given as $\mathrm{d}N/\mathrm{d}\log_{10} E_{rec}$ for two different declinations, $\delta = -30°$ (left column) and $\delta = 30°$ (right column) for background and an exemplary signal of an E^{-2} spectrum for the three different detector configurations, the 79-string configuration (top row), the 59-string configuration (middle row) and the 40-string configuration (bottom row).
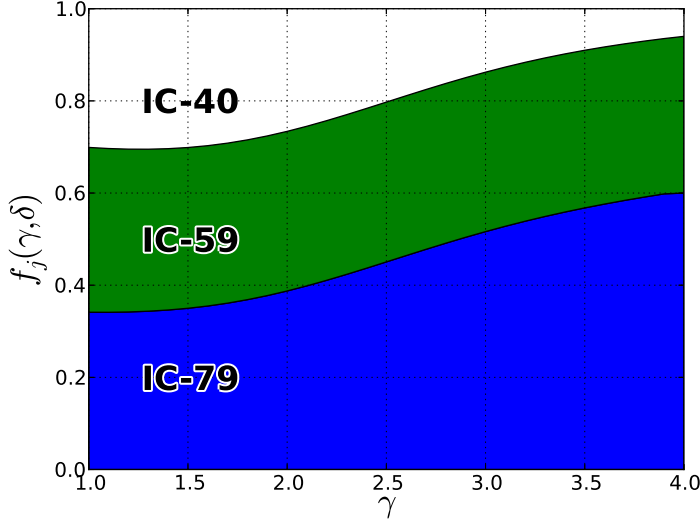
21

Figure 11: Relative efficiency or fraction of signal events coming from a source located at a declination of $+16°$ as a function of the spectral index for the three configurations. This relative efficiency is used as a weight in the likelihood method when combining multiple event selections.

sample while all other event properties such as the energy and declination are left unchanged. The fraction of the pseudo-experiments which yield a TS value above the observed TS is quoted as the p-value of the observation.

For the stacking searches we used the method described in Refs. [25, 11]. The signal p.d.f. is modified by breaking it into a sum over M sources. For one single sample the p.d.f can be re-written as:

$$\mathcal{S}_i \to \mathcal{S}_i^{tot} = \frac{\sum_{k=1}^{M} W^k R^k(\gamma, \delta_k)\mathcal{S}_i^k(|\vec{x}_i - \vec{x}_k|, \sigma_i)\mathcal{E}_i(E_i, \delta_i, \gamma)}{\sum_{k=1}^{M} W^k R^k(\gamma, \delta_k)}, \qquad (7)$$

where W^k is the relative theoretical weight for the k-th source in the catalog and $R^k(\gamma, \delta_k)$ is the detector acceptance for a flux with spectral index γ at the coordinates $\vec{x}_k$. The theoretical weights are chosen to minimize the flux required for discovery for a possible signal hypothesis. In catalogs where the predicted neutrino luminosity is strongly correlated with gamma-rays/X-ray/infrared fluxes we use these observations as a base for the theoretical weights. For catalogs with different possible theoretical flux predictions, the

22

sources can be weighted equally to maintain our sensitivity towards various signal hypothesis. The spectral index, γ, is assumed to be the same for all sources within a specific stacking search, and is a fit parameter along with the total number of signal events n_s.

The following is a description of all the searches performed with the three years of IceCube data (similar to those performed in Ref. [11]):

All-sky scan search. An all-sky search, where the likelihood is evaluated in each direction in the sky in steps of $0.1° \times 0.1°$ centered at the position of the source $\vec{x}_s$ over the declination range -85° to +85°. In this search the number of effective trials is very high and related to the number of positions in the grid. The significance of an excess found in some direction needs to be corrected for these trials.

A list of 44 selected sources. In order to reduce the large number of effective trials associated with scanning the entire sky, we also performed a search for the most significant of 44 *a priori* selected source candidates. This source list is selected according to observations in gamma-rays or astrophysical modeling predicting neutrino emission.

Stacking of 6 Milagro TeV gamma-ray sources. This catalogue is composed of most of the Milagro sources from [26] considered by the authors of Ref. [27] who estimated their neutrino emission. Given the observation in the IC-40 analysis of a significant *a posteriori* *p*-value from this catalogue, we considered a prescription for future samples and therefore the IC-40 data are not used in this analysis to avoid bias. Recent publications by the Milagro collaboration [29] ruled out some of the assumptions about gamma-ray fluxes used in Ref. [27] so we use an equal weight for each source in the likelihood, with the intention of keeping our sensitivity optimal for all possible signal hypothesis.

Stacking search for 127 local starburst galaxies. This search was already performed using IC-40 data [11]. Starburst galaxies are interesting as possible neutrino sources due to their high star formation rates, especially of high mass stars. The large amount of stars leads to lots of SNRs, possibly the sites of CRs acceleration below the knee. In [30] the authors associate the Far Infrared (FIR) emission with this hot ambient dust and the radio emission with synchrotron losses of electrons, which are assumed to be accelerated along with CRs in the large

number of SNRs. The high star formation rate is believed to be the underlying cause for the observed strong correlation between the FIR and the radio flux, and hence the neutrino fluxes are expected to follow a similar pattern. We perform a stacking search for the catalog of 127 starburst galaxies as compiled in Table A.1 in [30]. We use the FIR flux at 60 μm as the theoretical weight in the search hypothesis.

Stacking search for 5 nearby clusters of galaxies The stacking search for nearby clusters of galaxies, updated here after first results were presented in Ref. [11], is performed by testing four models assuming different CR spatial distribution within the source [31]. Clusters of galaxies are interesting potential sources of neutrinos that could be produced by interactions between high energy protons and the Intra Cluster Medium (ICM). In [31] the authors discuss four different spectral shapes for the possible neutrino emission from these sources, as characterized by four different models of CR distribution. The source extensions are different for each model for different sources and are modeled as 2 dimensional Gaussian distributions with the corresponding widths for each model. The differential fluxes predicted by [31] are parametrized as broken power laws as described in [11] and used as theoretical weights in the likelihood.

Stacking search for SNRs associated with molecular clouds. Molecular clouds surrounding SNRs can serve as target for high energy protons (or heavier nuclei) accelerated by SNR shocks to produce high energy gamma-rays and neutrinos. Specific models such as [36] suggest a high correlation between the expected gamma-ray and neutrino fluxes. We stack sources from a catalog of close molecular clouds associated with SNRs, which were observed at high energy by AGILE, Fermi, VER-ITAS, H.E.S.S. and MAGIC [32, 33, 34, 35]. The expected neutrino energies from these sources do not allow for a study in the Southern Hemisphere where this search has sensitivity to PeV - EeV energies. Only galactic sources in the northern sky, where IceCube is sensitive to TeV energies, were selected. The catalog contains 4 SNR associated with molecular clouds: W51C, W44, IC 443 and W49B. The integrated gamma-ray flux above 1 TeV for each source (in Crab units) is used as the theoretical weight in the likelihood. Very recently the Fermi collaboration detected the characteristic pion-decay signature in the

gamma-ray emission for two of these SNRs, IC 443 and W44, providing direct evidence that Cosmic Rays protons are accelerated in SNRs [37] at GeV energies.

Stacking search for galaxies with supermassive black holes. Ref. [38] systematically catalogs possible black hole candidates from within the Greisen-Zatsepin-Kuzmin limit [39] of around 100 Mpc. In order to keep only the most powerful emitters of particles, a cut of 5×10^8 solar masses is applied to the catalog to produce a final list of 233 sources. We use as weights the 2 micron Near Infrared flux from the 2 Micron All Sky Survey that can be related to the mass of black holes [38].

5. Results

The results of the all-sky scan are shown in the pre-trial significance map of p-values in Fig. 12. The most significant deviation in the northern sky has a pre-trial p-value of 1.96×10^{-5} and is located at 34.25° r.a. and 2.75° dec. Similarly, the most significant deviation in the southern sky has a pre-trial p-value of 8.97×10^{-5} and is located at 219.25° r.a. and $-38.75°$ dec.

The post-trial probabilities calculated as the fraction of scrambled sky maps with at least one spot with an equal or higher significance for each hemisphere correspond to 57% and 98% for the northern and the southern spots respectively and therefore both excesses are well compatible with the background hypothesis.

Figure 13 shows the p-value distribution for the hottest spot in the Northern Hemisphere (left) and for the Southern Hemisphere (right). The observed p-value in the data is indicated in both distributions, the final post-trial is given by integrating the right hand side of the distribution from the observed values.

The results of the point-source search in the direction of the 44 search selected *a priori* according to the positions of known objects is summarized in Tab. 2 and 3. The smallest p-value in the northern sky is found in the direction of HESS J0632+057 with a probability of 5.8%, however this value is translated into a post-trial probability of 65% once it is compared with an ensemble of randomized sky maps. For the southern sky, the highest significance is observed at the position of PKS 1454-354 with a pre-trial p-value of 23% which corresponds to a post-trial probability of 70%. The forth column of Tab. 2 and 3 shows the upper limits for an E^{-2} flux of $\nu_\mu + \bar{\nu}_\mu$
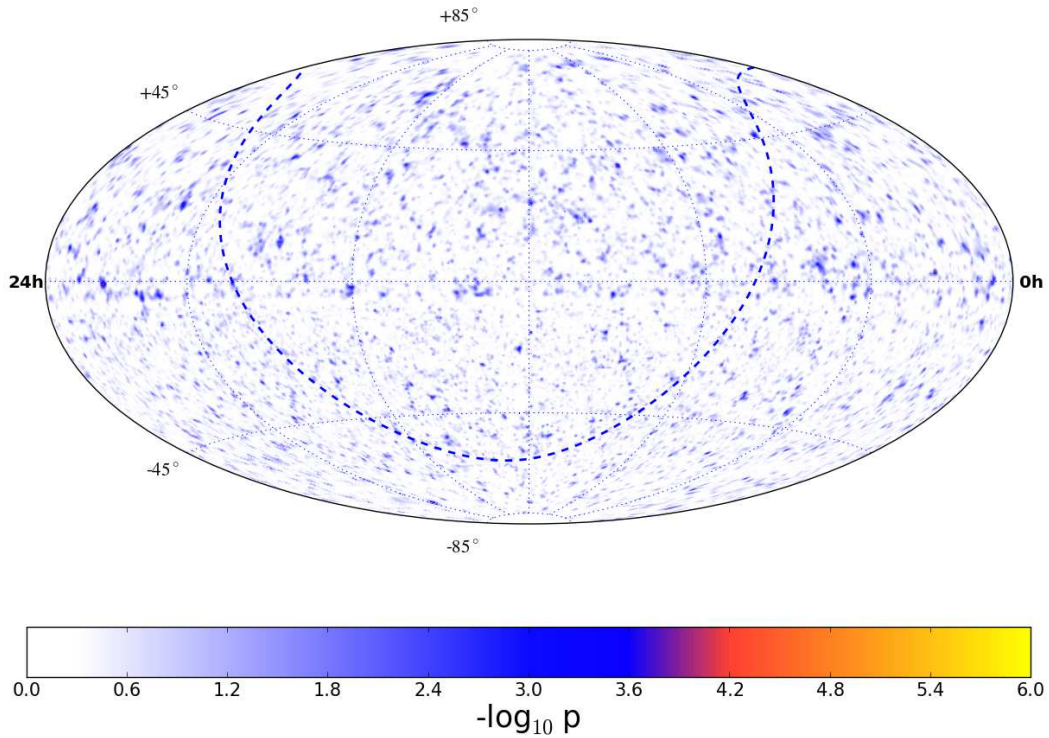
Figure 12: Pre-trial significance skymap in equatorial coordinates (J2000) of the all-sky point source scan for the combined IC79+IC59+IC40 data sample. The dashed line indicates the galactic plane.

calculated at 90% C.L. based on the classical (frequentist) approach [40] for each of the selected objects. The same values are indicated in Fig. 14 together with the IceCube sensitivity defined as the median upper limit and the discovery potential. Also shown are the ANTARES upper limits for a list of locations [41]
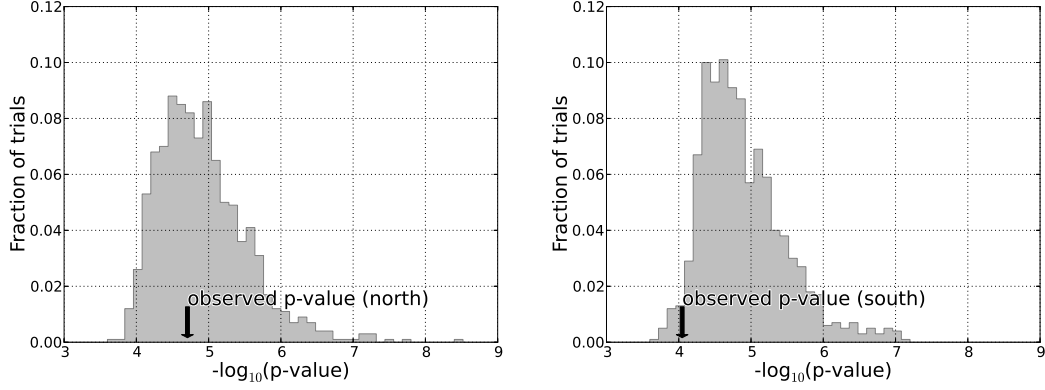
Figure 13: The distribution of the smallest *p*-value in the Northern (left) and the Southern (right) Hemisphere, obtained from randomized data. The observed *p*-values of the two hottest spots in the data are indicated by the two arrows.

Table 2: Results for galactic objects on the *a priori* search list.

Category	Source	r.a. [°]	dec. [°]	p-value	$\hat{n}_S$	$\hat{\gamma}$	$B_{1°}$	$\Phi^{90\%}_{\nu_\mu + \bar{\nu}_\mu}$
SNR	TYCHO	6.36	64.18	–	0.0	–	11.1	3.18
	Cas A	350.85	58.81	–	0.0	–	11.5	2.47
	IC443	94.18	22.53	0.43	2.8	3.9	17.2	1.63
HMXB /mqso	LSI +63 303	40.13	61.23	–	0.0	–	11.5	2.82
	Cyg X-3	308.11	40.96	0.43	2.5	3.9	12.9	2.35
	Cyg X-1	299.59	35.20	0.21	5.6	3.9	14.6	3.14
	HESS J0632+057	98.25	5.80	0.058^a	15.6	3.4	24.1	2.23
	SS433	287.96	4.98	–	0.0	–	24.3	0.92
Star Formation Region	Cyg OB2	308.08	41.51	–	0.0	–	12.7	1.87
pulsar/ PWN	MGRO J2019+37	305.22	36.83	–	0.0	–	14.3	1.83
	Crab Nebula	83.63	22.01	–	0.0	–	17.2	1.38

Table 2 – *Continued from previous page*

Category	Source	r.a. [°]	dec. [°]	p-value	$\hat{n}_S$	$\hat{\gamma}$	B$_{1°}$	$\Phi^{90\%}_{\nu_\mu+\bar{\nu}_\mu}$
	Geminga	98.48	17.77	–	0.0	–	19.5	1.193
Galactic Center	Sgr A*	266.42	-29.01	0.49	0.6	3.7	25.2	13.94
Not identified	MGRO J1908+06	286.98	6.27	–	0.0	–	23.8	1.00

Note. – Sources are grouped according to their classification as High-Mass X-ray binaries or micro-quasars (HMXB/mqso), SNRs, Pulsar Wind Nebulas (PWNs), star formation regions and unidentified sources. The p-value is the pre-trial probability of compatibility with the background-only hypothesis. The $\hat{n}_S$ and $\hat{\gamma}$ columns give the best-fit number of signal events and spectral index of a power-law spectrum. When $\hat{n}_S = 0$ no p-value or $\hat{\gamma}$ are reported. The eighth column gives the number of background events in a circle of 1° around the search coordinates. The last column shows the upper limits based on the classical approach [40] for an E^{-2} flux normalization of $\nu_\mu + \bar{\nu}_\mu$ flux in units of 10^{-12} TeV^{-1} cm^{-2}s^{-1}.

[a]Most significant p-value in the northern sky among all galactic and extragalactic objects on the *a priori* search list.

Table 3: Results for extragalactic objects on the *a priori* search list.

Category	Source	r.a. [°]	dec. [°]	p-value	$\hat{n}_S$	$\hat{\gamma}$	B$_{1°}$	$\Phi^{90\%}_{\nu_\mu+\bar{\nu}_\mu}$
BL Lac	S5 0716+71	110.47	71.34	–	0.0	–	10.3	3.60
	1ES 1959+650	300.00	65.15	0.19	5.7	3.9	11.1	5.53
	1ES 2344+514	356.77	51.70	0.29	4.7	3.9	12.4	3.32
	3C66A	35.67	43.04	–	0.0	–	12.7	1.86
	H 1426+428	217.14	42.67	–	0.0	–	12.7	1.90
	BL Lac	330.68	42.28	0.42	3.7	3.3	12.7	2.16
	Mrk 501	253.47	39.76	0.34	4.8	3.9	13.4	2.84
	Mrk 421	166.11	38.21	0.18	3.7	1.8	13.7	3.45

Table 3 – *Continued from previous page*

Category	Source	r.a. [°]	dec. [°]	p-value	$\hat{n}_S$	$\hat{\gamma}$	B_{1°	$\Phi^{90\%}_{\nu_\mu+\bar{\nu}_\mu}$
	W Comae	185.38	28.23	0.21	2.8	1.8	16.1	2.74
	1ES 0229+200	38.20	20.29	0.19	8.2	3.9	17.8	2.43
	PKS 0235+164	39.66	16.62	–	0.0	–	19.9	1.30
	PKS 2155-304	329.72	-30.23	–	0.0	–	25.5	14.28
	PKS 0537-441	84.71	-44.09	–	0.0	–	23.8	23.27
FSRQ	4C 38.41	248.81	38.13	–	0.0	–	13.7	1.76
	3C 454.3	343.49	16.15	–	0.0	–	19.9	1.23
	PKS 0528+134	82.73	13.53	–	0.0	–	20.8	1.14
	PKS 1502+106	226.10	10.49	0.076	8.4	2.3	21.2	2.40
	3C 273	187.28	2.05	–	0.0	–	25.0	0.90
	3C279	194.05	-5.79	–	0.0	–	23.5	2.06
	QSO 2022-077	306.42	-7.64	–	0.0	–	23.2	2.47
	PKS 1406-076	212.24	-7.87	–	0.0	–	23.2	2.49
	QSO 1730-130	263.26	-13.08	–	0.0	–	25.6	5.04
	PKS 1622-297	246.53	-29.86	0.45	0.7	4.0	25.2	16.91
	PKS 1454-354	224.36	-35.65	0.23^b	1.0	5.9	24.1	29.89
Starburst	M82	148.97	69.68	–	0.0	–	10.7	4.00
Radio Galaxies	NGC 1275	49.95	41.51	–	0.0	–	12.7	1.91
	Cyg A	299.87	40.73	0.15	1.5	1.5	12.9	3.82
	Cen A	201.37	-43.02	0.46	2.0	1.4	23.9	26.62

Continued on next page

Table 3 – *Continued from previous page*

Category	Source	r.a. [°]	dec. [°]	p-value	$\hat{n}_S$	$\hat{\gamma}$	B_{1°	$\Phi^{90\%}_{\nu_\mu+\bar{\nu}_\mu}$
	3C 123.0	69.27	29.67	–	0.0	–	15.9	1.57
	M87	187.71	12.39	0.45	2.9	–	20.9	1.37

Note. – Sources are grouped according to their classification as BL Lac objects, Radio Galaxies, Flat-Spectrum Radio Quasars (FSRQ) and Starburst galaxies. The p-value is the pre-trial probability of compatibility with the background-only hypothesis. The $\hat{n}_S$ and $\hat{\gamma}$ columns give the best-fit number of signal events and spectral index of a power-law spectrum. When $\hat{n}_S = 0$ no p-value or $\hat{\gamma}$ are reported. The eighth column gives the number of background events in a circle of 1° around the search coordinates. The last column shows the upper limits based on the classical approach [40] for an E^{-2} flux normalization of $\nu_\mu + \bar{\nu}_\mu$ flux in units of 10^{-12} TeV^{-1} cm^{-2}s^{-1}.

[b]Most significant p-value in the southern sky among all galactic and extra-galactic objects on the *a priori* search list.

The 6 Milagro TeV sources stacking analysis resulted in a post-trial p-value of 20.4% with a best fit $\hat{n}_s = 17$. In the GC stacking searches, less events than expected from the background were observed for all of the four models tested, meaning that the p-value is at least $\geq 50\%$. Also the SNRs associated with Molecular Clouds as well as the Starburst galaxies resulted both in negative fluctuations of the background in every case with $\hat{n}_s = 0$. Finally the black hole stacking search produced a post-trial p-value of 44.3% with 12 signal events as the best fit.

5.1. Implications for models of astrophysical neutrinos.

This analysis has shown that there is no evidence of neutrino emission from point-sources in the sky. In the absence of a positive detection it is, however, possible to constrain some models that predict astrophysical neutrino emissions. IceCube is entering a new stage in which a non-discovery has meaningful implications and can provide insight about the nature of these phenomena. IceCube has provided the most constraining upper limits on neutrino fluxes from sources like the Crab [17]. Even though the Crab spectral
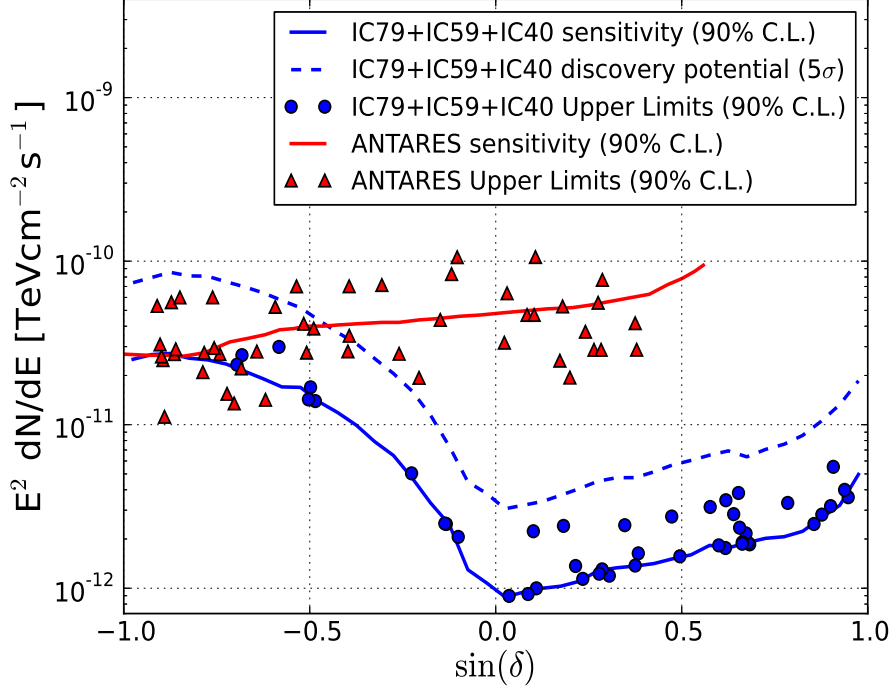
Figure 14: Muon neutrino and antineutrino flux 90% C.L. upper limits and sensitivities for an E^{-2} spectrum. Published limits of ANTARES [41] are shown. The different likelihood function and method to derive upper limits used by ANTARES may account for differences in the limits from the two experiments at the level of 20%. In the case of the IceCube method, negative values of the number of signal events are not allowed in the minimization procedure. Therefore for those sources where there was an under-fluctuation of the background the upper limit matches the median upper limit.

emission seems to be fully explained by electromagnetic phenomena, several γ-ray flares observed in the past years in the GeV region ($E_\gamma > 100$ MeV) challenge purely leptonic models [46]. The impact of IceCube limits on different models of neutrino emission from the Crab was already discussed in [17] for the 40-string configuration of IceCube. Here we update the upper limits based on this three year analysis of IceCube. Figure 15 summarizes a number of different predicted muon neutrino fluxes at Earth according to several models (standard oscillations have been taken into account). The green solid line corresponds to the flux predicted in [42] based on the γ-ray spectrum measured by H.E.S.S. As can be seen, the IceCube upper limit is only a
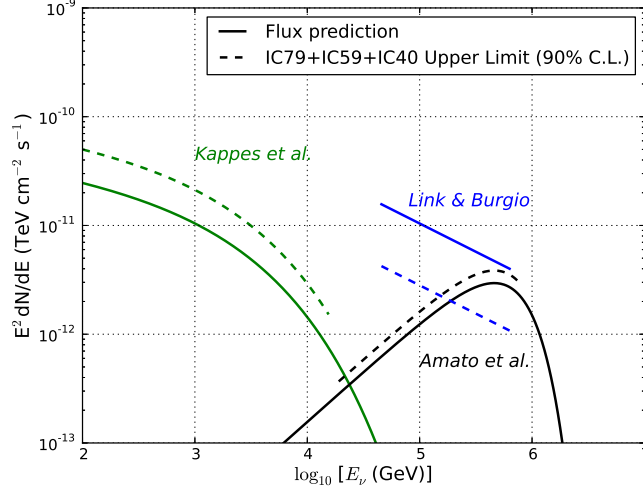
Figure 15: Predicted muon neutrino fluxes for several hadronic models for steady neutrino emission from the Crab and upper limits based on 3 years of IceCube data. Solid lines indicates the flux prediction and the dashed lines the corresponding upper limit flux for a 90% C.L. for an energy range that contains 90% of the signal. Neutrino oscillations are accounted for.

factor of two above the flux prediction. This is interesting since it indicates that neutrino astronomy is at the level of sensitivity of gamma astronomy experiments (the factor of two corresponds to the muon neutrino flux lost due to oscillations along the path from the source). The black line represents the estimated flux based on the resonant cyclotron absorption model. In Ref. [43] inelastic nuclear collisions are considered and the predicted neutrino rates depend on the Lorentz factor, Γ, of nuclei injected by the pulsar and the effective target density. The predicted flux in Fig. 15 is for the most optimistic case of the effective target density and a wind Lorentz factor of $\Gamma = 10^7$. Ref [44, 45] considers scattering of wind protons with the X-ray emission from the pulsar's surface. The predicted neutrino flux assuming a quadratic scaling of the proton's energy with the height above the surface is shown in the plot. The most optimistic version of this model can be rejected with more than 90% C.L.

IceCube upper limits are approaching to some predictions from models on neutrino emission from SNRs. In [14] the authors calculate the neutrino spectra generated by proton-proton interactions at supernova remnants. For

the Northern Hemisphere, the G40.5-0.5 seems to be the most promising candidate for a neutrino detection due to the high photon flux from this source. The electron spectrum of this supernova remnant is supposed to cut off at energies lower than the measured radiation, indicating a possible hadronic origin of the radiation. Figure 16 shows the different predicted muon neutrino spectra after considering oscillations for three SNRs. The 90 % C.L. flux upper limit for muon neutrinos is also shown.
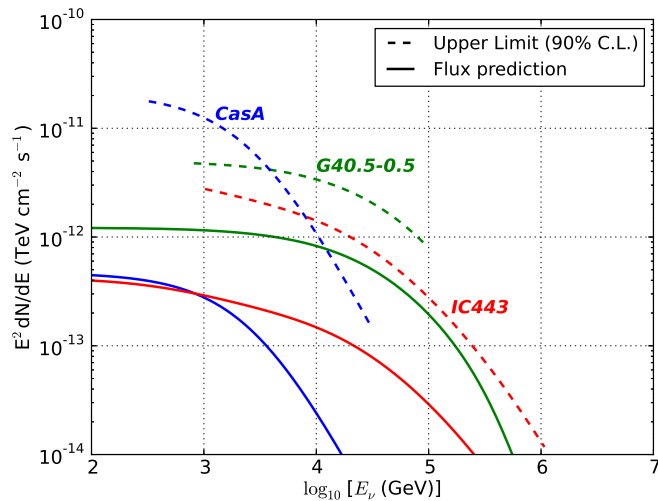

Figure 16: Predicted muon neutrino fluxes from three modeled SNRs in the Northern Hemisphere according to 16. The muon neutrino 90% C.L. upper limits from this analysis are shown in the energy range of the 90% signal containment.

As can be seen, IceCube upper limits in the most optimistic case, for the G40-5.0.5, are still a factor of four above the flux prediction. However, stacking techniques can improve the discovery potential. Figure 17 shows the upper limit of the stacking result of the 6 Milagro TeV gamma-ray associations assuming the model from [27]. The result of the analysis was a positive fluctuation, so the sensitivity is expected to be closer to the total predicted flux than the upper limit. Together in this plot we show the flux prediction and the corresponding upper limit from the 5 nearby galaxy clusters search assuming that CRs are uniformly distributed within the virial radius of the galaxy cluster.
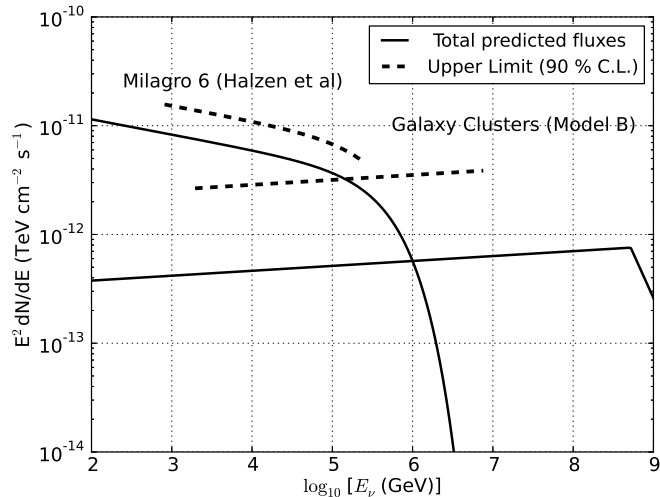
33

Figure 17: Predicted muon neutrino fluxes from 6 Milagro sources in gamma-rays according to [27] and from the 5 nearby galaxy clusters considered in [31]. The corresponding 90% C.L. flux upper limit for muon neutrinos obtained from the stacking analysis are shown as well.

6. Systematic Uncertainties

One of the strengths of the presented searches is that they use a data-driven background estimation based on randomized data. The p-values are unaffected by uncertainties on the theoretical estimate of fluxes of the background of atmospheric neutrinos and muons that depend on hadronic models of shower development in the atmosphere and on the CR composition. They are also unaffected by the poorly known contribution of prompt neutrinos. Moreover, uncertainties on the simulation of the detector also do not affect the post-trial p-value.

On the other hand upper limits are affected by the systematic errors on the simulation of the detector efficiency and response to the flux of neutrinos. The construction of the signal energy density function in the likelihood method depends on simulation and is therefore affected by the systematic uncertainties. In order to capture the impact of the systematic uncertainties, we fully propagated each of them through the likelihood search and calculated the sensitivity of the search for a discrete set of simulated signal responses within the allowed range of uncertainties. We used the IC-79 data sample for this evaluation and we quote the declination-averaged uncertainties under

34

the assumption that all samples are affected by the same systematic errors. This assumption can be regarded as conservative since the lower energy range is more strongly affected by the uncertainties and the IC-79 sample contains the largest number of low energy events.

The two most relevant uncertainties come from the absolute efficiency of the optical modules and the modeling of the optical properties of the ice. As a conservative estimate, we allowed for a $\pm 10\%$ uncertainty in the absolute efficiency of the optical modules. Uncertainties in the relative sensitivity of the individual DOMs with respect to the detector average have been observed to have a negligible impact on the total flux uncertainty in the energy range of this analysis. Likewise, there is no significant impact if the sensitivity of the high quantum efficiency PMTs in DeepCore [6] is larger with respect to the rest of the detector. This is due to the limited size of this part of the detector with respect to the typical track length of the event selected in this analysis. The uncertainty of $\pm 10\%$ in DOM efficiency in simulation resulted in $+6\%/-7\%$ variation in the sensitivity of IC-79. The parametrization of the optical properties of the ice used in this work is a variant of the parametrization presented in [49]. Its uncertainties have been taken to be $\pm 10\%$ in absorption and scattering and they both have been rescaled at the same time. The effect in sensitivity coming from these variation was of $+5\%/-8\%$.

Due to constraints in computing power, we used tabulated photon arrival probabilities in the signal simulation [48]. A more accurate description of the detector response can be obtained by using simulation with direct photon propagation [47]. The difference between the two is most relevant for energies below ~ 1 TeV and decreases with energy. In order to quantify the impact of the photon propagation method, we compared the difference in sensitivity in the northern sky using simulated data generated specifically for this purpose. The impact on the Southern Hemisphere is expected to be smaller and the values for the northern sky do thus represent a conservative estimate for the full sky. The difference in sensitivity, 7.2%, between the two propagators can be accounted for by the uncertainty in the optical efficiency and therefore here is not considered as an additional source of systematic uncertainty. Future simulations of IceCube are expected to be produced with direct photon propagation while an increase in the nominal optical efficiency of 10% is also foreseen since a higher optical efficiency was found to better describe IceCube data.

There is a small probability that southern sky signal neutrinos are vetoed by the IceTop veto applied in the IC-79 and IC-59 data samples due to

random coincidences. As can be seen in Figure 6 on the left, this probability for random coincidences is constantly below 1% at all declinations and can therefore be neglected in comparison to the impact of other systematic uncertainties.

By summing in quadrature all the different contribution the expected uncertainty in the IC-79 sensitivity is about 18%. This is compatible with the 16% estimated for the IC-40 configuration [11].

The upper limits listed in the previous section have been calculated for a pure muon neutrino signal, under the assumption that no other neutrino flavors contribute in this analysis. Considering neutrino oscillations with a large mixing angle $\Theta_{23} \sim 45°$ and a long baseline, a typical neutrino flavor ratio of ν_e:ν_μ:ν_τ = 1:2:0 at the source will result in an approximate partition of 1:1:1 at Earth. In the case of ν_τ the resulting τ will decay into a μ with a branching ratio of about 17%. These additional muons from ν_τ can contribute to a possible signal flux in this analysis. In [11], the contribution of ν_τ in addition to the ν_μ flux simulated in this work has been determined to be $10 - 16\%$ of the ν_μ contribution.

7. Conclusions

We present the results of the point source analysis of three years of data with the 40-string, 59-string and 79-string configurations of the IceCube Neutrino Observatory. The combined data has a total live-time of 1,040 days from April 2008 to May 2011. The all-sky survey found no evidence of point-source neutrino emission in the Northern or the Southern Hemisphere. The post-trial probabilities of the highest significant coordinate in each hemisphere are compatible with background fluctuations. Additionally, a search on a catalog of known emitters of high-energy radiation was performed. Several stacking analyses were carried out to integrate the possible signal from all sources of the same class. Also in this case, no significant deviation from the background hypothesis was found and the corresponding 90% C.L. upper limits on the muon neutrino fluxes were calculated and compared to predictions. The most optimistic models considered here can be excluded at 90% C.L. and in other cases limits are factor two to four above the predictions.

The muon neutrino upper limits presented here improve earlier results [11] by a factor ~ 3.5 or better and are the strictest neutrino limits to date over the entire sky. Some of these limits for an E^{-2} muon neutrino flux have reached the level of 10^{-12} TeV cm^{-2}s^{-1} necessary to test current models of

neutrino emission expected for galactic sources like supernova remnants [50]. In the future, the sensitivity of IceCube to neutrino point source will improve with the inclusion of additional data collected with the full IceCube array.

Appendix A. Muon neutrino effective area

Table A.4 presents the tabulated values of the solid-averaged muon neutrino effective for the three different configurations used in this analysis:

Table A.4: Muon neutrino effective areas.

$\log_{10} E_{min}$	$\log_{10} E_{max}$	North ($0° < \delta \leq 90°$)			South ($-90° \leq \delta \leq 0°$)		
		IC-79	IC-59	IC-40	IC-79	IC-59	IC-40
3.00	3.25	0.41	0.28	0.12	0.02	0.01	0.00
3.25	3.50	1.11	0.78	0.34	0.06	0.04	0.01
3.50	3.75	2.65	2.01	1.07	0.17	0.11	0.04
3.75	4.00	5.87	4.65	2.56	0.46	0.32	0.11
4.00	4.25	11.83	9.58	5.52	1.05	0.78	0.34
4.25	4.50	21.77	18.36	12.00	2.52	1.83	0.74
4.50	4.75	36.99	31.67	22.86	5.36	3.74	1.83
4.75	5.00	58.47	50.86	34.85	10.88	7.99	3.26
5.00	5.25	87.14	76.92	55.80	21.77	15.87	7.87
5.25	5.50	121.76	108.50	81.50	42.85	30.24	15.34
5.50	5.75	160.62	144.95	110.00	80.52	57.23	27.82
5.75	6.00	205.52	187.38	141.89	147.57	106.95	53.59
6.00	6.25	251.32	228.80	181.35	237.05	175.87	95.41
6.25	6.50	300.92	280.14	216.07	360.95	275.64	172.67
6.50	6.75	349.98	335.04	270.26	511.18	402.76	251.98
6.75	7.00	406.74	379.00	298.75	701.98	549.56	366.78
7.00	7.25	452.88	440.70	358.44	949.45	759.58	498.23
7.25	7.50	497.98	481.35	419.92	1248.55	999.85	649.27
7.50	7.75	561.75	531.64	482.86	1623.10	1324.28	834.44
7.75	8.00	603.41	596.59	488.16	2084.37	1709.82	993.06
8.00	8.25	660.84	660.13	535.53	2642.73	2164.94	1297.21
8.25	8.50	719.94	732.64	520.84	3353.95	2779.39	1453.31

Continued on next page

37

Table A.4 – *Continued from previous page*

		North ($0° < \delta \leq 90°$)			South ($-90° \leq \delta \leq 0°$)		
$\log_{10} E_{min}$	$\log_{10} E_{max}$	IC-79	IC-59	IC-40	IC-79	IC-59	IC-40
8.50	8.75	774.93	780.96	648.86	4227.17	3443.88	1608.56
8.75	9.00	813.21	839.18	632.89	5307.43	4261.46	1746.93

Note. – Solid-angle-averaged neutrino effective area for $\nu_\mu + \bar{\nu}_\mu$ in the north and south skies. The first two columns indicates the limits of the energy bin so that $\log_{10}[E_{min}] < \log_{10}[E_\nu(\text{GeV})] \leq \log_{10}[E_{max}]$. The muon neutrino effective area is shown in units of m^2 for each of the three configurations.

References

[1] J. G. Learned & K. Mannheim, Ann. Rev. of Nucl. and Part. Sci. **50** (2000) 679.

[2] J. K. Becker, Phys. Rep. **458** (2008) 173.

[3] R. Abbasi *et al.* [IceCube Coll.], *Search for flares and periodic signals from astrophysical neutrino sources with 3 years of IceCube* in preparation.

[4] R. Abbasi *et al.* [IceCube Coll.], Nucl. Inst. Meth. A **618** (2010) 139.

[5] R. Abbasi *et al.* [IceCube Coll.], Nucl. Inst. Meth. **A601** (2009) 294 [arXiv:0810.4930].

[6] R. Abbasi *et al.* [IceCube Coll.], Astropart. Phys. **35** (2012) 615.

[7] A. R. Bell, Mon. Not. Roy. Astron. Soc. **182** (1978) 147.

[8] R. Schlickeiser, Astrop. J. **336** (1989) 243.

[9] R. Abbasi *et al.* [IceCube Coll.], Nucl. Inst. Meth. A **700** (2013) 188 [arXiv:1207.6326].

[10] R. Abbasi *et al.* [IceCube Coll.], Phys. Rev. **D83** (2011) 012001.

[11] R. Abbasi *et al.* [IceCube Coll.], Astrop. J. **732** (2011) 18.

[12] J. Ahrens *et al.* [AMANDA Coll.], Nucl. Inst. Meth. **A524** (2004) 169.

[13] R. Abbasi *et al.* [IceCube Coll.], Nucl. Inst. Meth. A **703** (2013) 190.

[14] M. Manderlartz & J. Becker Tjus, subm. to Astrop. J. (2013) [arXiv:1301.2437].

[15] P. H. Barret *et al.*, Rev. Mod. Phys. **24** (1952) 133.

[16] R. Abbasi *et al.* [IceCube Coll.], Astrop. J. **763** (2013) 33.

[17] R. Abbasi *et al.* [IceCube Coll.], Astrop. J. **745** (2012) 45.

[18] T. Neunhöffer, Astropart. Phys. **25** (2006) 220.

[19] S. S. Kerthi *et al.*, Neural Comp., **13** (2001) 637.

[20] T. Hastie, R. Tibshirani and J. H. Friedman, The elements of statistical learning: data mining, inference, and prediction, New York: Springer-Verlag (2009).

[21] R. Abbasi *et al.* [IceCube Coll.], Phys. Rev. Lett. **103** (2009) 221102.

[22] J. Auffenberg *et al.* [IceCube Coll.], in *Proc. of the* 32nd Int. Cosmic Ray Conf., Beijing, China (2011) [arXiv:1111.2736].

[23] M. Honda *et al.*, Phys. Rev. **D75** (2007) 043006.

[24] J. Braun *et al.*, Astropart. Phys. **33** (2010) 175.

[25] A. Achterberg *et al.*, Astropart. Phys. **26** (2006) 282.

[26] A. A. Abdo *et al.*, Astrop. J. **664** (2007) L91.

[27] F. Halzen, A. Kappes and A. O'Murchadha, Phys. Rev. **D78** (2008) 063004.

[28] A. A. Abdo *et al.*, Astrop. J. **700** (2009) L127.

[29] A. A. Abdo *et al.*, Astrop. J. **753** (2012) 159.

[30] J. Becker *et al.* (2009) arXiv:0901.1775.

[31] K. Murase *et al.*, Astrop. J. Lett. **689** (2008) L105.

[32] A. A. Abdo *et al.* [Fermi Coll.], Astrop. J. Lett. **706** (2009) L1.

[33] A. A. Abdo *et al.* [Milagro Coll.], Astrop. J. Lett. **700** (2009) L127.

[34] A. Fiasson *et al.* [HESS Coll.], in *Proc. of the* 31st Int. Cosmic Ray Conf., Lodz, Poland (2009).

[35] A. A. Abdo *et al.* [Fermi Coll.], Science **327** (2010) 1103.

[36] V. Cavasinni *et al.*, Astropart. Phys. **26** (2006) 41.

[37] M. Ackermann *et al.* [Fermi Coll.], Science **339** (2013).

[38] L. Caramete & P.L. Biermann, Astron. Astrophys. **521** (2010) A55.

[39] K. Greisen, Phys. Rev. Lett. **16** (1966) 748; G. T. Zatsepin, & V. A. Kuz'min, J. of Exp. and Theor. Phys. Lett. **4** (1966) 78.

[40] J. Neyman. Phil. Trans. Royal Soc. London A **236** (1937) 333.

[41] S. Adrián-Martínez *et al.* [ANTARES Coll.], Astrop. J. Lett. **743** (2011) L14.

[42] A. Kappes *et al.*, Astrophys. J. **656** (2007) 870.

[43] E. Amato, D. Guetta and P. Blasi, Astron. Astrophys. **402** (2003) 827.

[44] B. Link & F. Burgio, Phys. Rev. Lett. **94** (2005) 181101.

[45] B. Link & F. Burgio, Mon. Not. Roy. Astron. Soc. **371** (2006) 375 [astro-ph/0604379].

[46] A. A. Abdo *et al.*, Science **331** (2011) 739.

[47] D. Chirkin *et al.* [IceCube Coll.], Nucl. Inst. Meth. A. doi:10.1016/j.nima.2012.11.170.

[48] J. Lundberg *et al.*, Nucl. Inst. Meth. A **581** (2007) 619.

[49] R. Abbasi *et al.* [IceCube Coll.], Nucl. Inst. Meth. A. **711** (2013) 73.

[50] F. Vissani *et al.* Astropart. Phys. **34** (2011) 778.